Alkylated and restored graphene oxide nanoribbon-reinforced isotactic-polypropylene nanocomposites

Min Yeong Song [a], [1], Se Youn Cho [a], [1], Na Rae Kim [a], Seok-Heon Jung [a], Jin-Kyun Lee [a], Young Soo Yun [b], [**], [1], Hyoung-Joon Jin [a], [*], [1]

[a] Department of Polymer Science and Engineering, Inha University, Incheon 402-751, Republic of Korea
[b] Department of Chemical Engineering, Kangwon National University, Samcheok 245-711, Republic of Korea

ARTICLE INFO

ABSTRACT

Nanostructured carbon materials have outstanding physical properties and high aspect ratios. They have attracted much attention for use as polymer composite reinforcements. In this study, alkylated and reduced graphene oxide nanoribbons (A-rGONRs) were prepared by unzipping multi-walled carbon nanotubes (MWCNTs), followed by a simple alkylation/chemical reduction process using a Dean-Stark trap. A-rGONRs have morphologies with width 30—50 nm and lengths of several micrometers (aspect ratio >100). They are similar to one-dimensional MWCNTs, but with extended interfacial areas and edge functional sites. Approximately 25 wt% of the alkyl chains were chemically introduced onto the surface of A-rGONRs, which gave rise to hydrophobic properties and a surface energy of 23.8 mJ m^{-2}. A stable A-rGONRs suspension was achieved in xylene even after 24 h. Through a wet process, A-rGONRs were homogeneously dispersed in an isotactic polypropylene (iPP) host. iPP/A-rGONRs nanocomposites showed significant enhancements in thermal and mechanical properties when compared to pure iPP.

© 2016 Elsevier Ltd. All rights reserved.

1. Introduction

Nanostructured carbon materials (NCMs) such as carbon nanotubes (CNTs) and graphene have attracted great attention for use as polymer composite reinforcements due to their unique characteristics [1—6], including high mechanical strength (>1060 GPa for graphene; > 63 GPa for CNTs) [2,3], high thermal conductivity (~3000 W mK^{-1} for graphene; ~6000 W mK^{-1} for CNTs) [4,5], and high specific surface area (~2600 m^2 g^{-1} for graphene; ~216 m^2 g^{-1} for CNTs) [4,6]. Several reports show enhancements in the mechanical and thermal properties of host polymers through the addition of small amounts of NCMs [7—14]. In addition, NCMs have high surface energy and a tendency to aggregate [15,16]. NCMs aggregated in a polymer matrix significantly decrease the properties of the nanocomposites [17]; therefore, strong interfacial adhesion and homogeneous dispersion of NCMs in a polymer host are some of the key factors to consider when maximizing their

reinforcing effects. The physical attachment of aromatic-containing molecules via $\pi-\pi$ stacking on the surface of NCMs can be an effective and simple method for their dispersion in organic solvents and/or a polymer matrix; however, the physical bonding is too weak to efficiently transfer load from the polymer to the NCMs [18—20]. In contrast, attaching polymer/oligomer molecules or alkyl chains onto the plane of NCMs by direct grafting or alkylation, respectively creates strong chemical bonding [21—23], leading to the homogeneous dispersion of NCMs and efficient load transfer. In general, chemical modifications have been achieved using oxygen functionalized NCMs prepared via a chemical route [24—26].

Graphene nanoribbons (GNRs) are one-dimensional carbon strips composed of an sp^2 hexagonal carbon structure with larger interfacial areas and more numerous edge sites compared to CNTs [27,28]. Stronger interfacial adhesion to a polymer matrix can therefore be achieved in GNR-reinforced nanocomposites. In addition, the aspect ratio of GNRs is high enough (>100, length:-width) that a percolation threshold can be induced by a small number of GNRs, which is lower than that for graphene [29].

Oxygen functionalized GNRs (GONRs) can be prepared by unzipping CNTs [28]. GONRs have good dispersibility and strong interfacial adhesion in a hydrophilic polymer matrix, which leads to a significant enhancement in the physical properties of the epoxy

---

* Corresponding author.
** Corresponding author.
E-mail addresses: ysyun@kangwon.ac.kr (Y.S. Yun), hjjin@inha.ac.kr (H.-J. Jin).
[1] These authors contributed equally to this work.

[30]. In addition, through surface modification of GONRs using alkyl chains, alkylated GONRs (A-GONRs) can be effective as a reinforcement in hydrophobic polymer hosts [31]; however, the defective carbon structure of GONRs or A-GONRs results in decay of their reinforcing effects in glassy polymers [32,33]. Therefore, both the restoration of the defective carbon structure and the introduction of alkyl chains are required to create an efficient reinforcing effect in GONR-based nanocomposites. Tour et al. reported hexadecyl-functionalized low-defect GNRs (HD-GNRs) produced from *in situ* intercalation of Na/K alloy into CNTs, followed by quenching with 1-iodohexadecane [34,35]. The incorporation of HD-GNRs in a thermoplastic polyurethane matrix led to dramatic enhancement of its mechanical properties [35]. In addition, Regev et al. reported that edge functionalized low-defect GNRs treated with polyvinylamine chains showed effective reinforcing behaviors including fracture toughness, flexural strength, and shear strength in an epoxy polymer matrix [36]. These reports are good examples of the reinforcing potential of GNRs-based polymer nanocomposites. There is, however, no information about the reinforcing effects of A-GNRs/A-GONRs on a polyolefin matrix, which is one of the most widely used polymers in industry.

In this study, alkylated and reduced GONRs (A-rGONRs) were fabricated via a one-step reduction and alkylation process and their reinforcing effects in an isotactic polypropylene (iPP) matrix were investigated by adding 0, 0.05, 0.1, and 0.3 wt% A-rGONRs. To produce an iPP nanocomposite via a wet process using high temperature xylene, a new method using a Dean-Stark trap was developed, which combined the alkylation, reduction, and dispersion of GONRs in xylene and the homogeneous mixing of iPP and A-rGONRs into one step. For polyolefin-based nanocomposites in particular, the reported alkylation and reduction methods require several steps. The new method facilitates homogeneous dispersion of A-rGONRs in the iPP matrix as well as *in situ* alkylation and reduction of GONRs. The iPP/A-rGONRs nanocomposites showed improvements of ~98.0%, 14.6%, 31.4%, and 43.5% in the Young's modulus, tensile strength, elongation, and toughness, respectively. In addition, the thermal degradation temperature (T_d) and crystallization temperature (T_c) of the iPP/A-rGONRs nanocomposites increased by ~31 °C and 2.9 °C, respectively. This study provides information about a simple alkylation/reduction method for A-rGONRs and their effects on the reinforcement of an iPP matrix.

2. Experimental

2.1. Preparation of GONRs

GONRs were prepared according to a previously reported method [28]. Briefly, 150 mg of multi-walled CNTs (MWCNTs, 95%, Hanwha Nanotech Inc., Korea) were treated in concentrated sulfuric acid for 12 h, and 750 mg of KMnO$_4$ was added into the solution. The reaction mixture was stirred at room temperature for 1 h, and then heated to 55—70 °C for an additional 1 h. The reaction mixture was poured into 400 mL of ice containing 50 mL of 30% H$_2$O$_2$. The solution was filtered using a polytetrafluoroethylene membrane, and washed with distilled water. The synthesized GONRs were dispersed in distilled water and frozen at −196 °C. The samples were then freeze-dried at −50 °C and 0.0045 mbar for 72 h. The resulting GONRs were stored in a vacuum oven at 30 °C.

2.2. Preparation of A-rGONRs

For the iPP/A-rGONRs nanocomposites, 7.5, 15, and 45 mg of GONR powders were dispersed in 40 mL of distilled water via ultrasound treatment (power and frequency of 200 W and 20 kHz, respectively) in a round-bottom flask. Then, 0.1 g of octylamine (99%, Sigma-Aldrich) and 40 mL of xylene (98.5%, Duksan) were added to the round-bottom flask. A Dean-Stark trap was used for the preparation of A-rGONRs, as shown in Fig. S1. The solution mixture was stirred in a 130 °C silicon oil bath for 12 h. A homogeneous A-rGONRs dispersion in xylene was obtained. For comparison, rGONRs were prepared by hydrazine treatment according to a reported method [37].

2.3. Preparation of iPP/A-rGONRs nanocomposites

First, 15 g of iPP (M$_w$ ~250,000, M$_n$ ~67,000, Sigma-Aldrich) was dissolved in xylene at 130 °C in a three-necked round-bottom flask. The homogeneous A-rGONRs dispersion was then poured into the iPP solution and stirred for 30 min. Subsequently, the nanocomposite solution was poured into a methanol bath to precipitate the iPP/A-rGONRs nanocomposites. The precipitate was vacuum-filtered and washed with methanol several times. The resultant iPP/A-rGONRs nanocomposites were dried at 70 °C for 48 h and
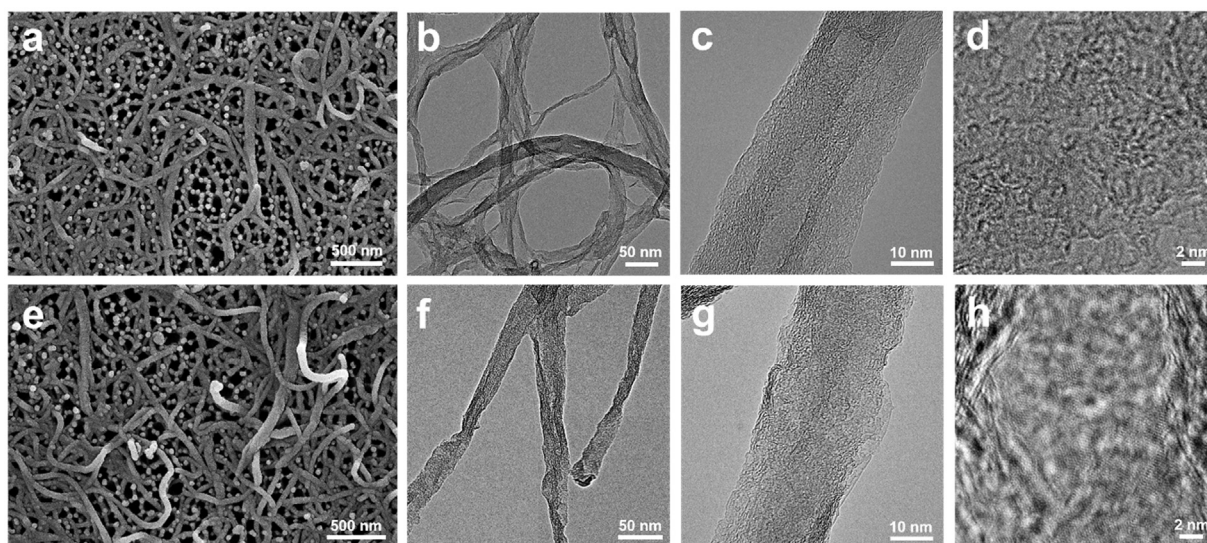

Fig. 1. FE-SEM images of (a) GONRs and (e) A-rGONRs. FE-TEM images of (b), (c), (d) GONRs and (f), (g), (h) A-rGONRs with various magnifications.
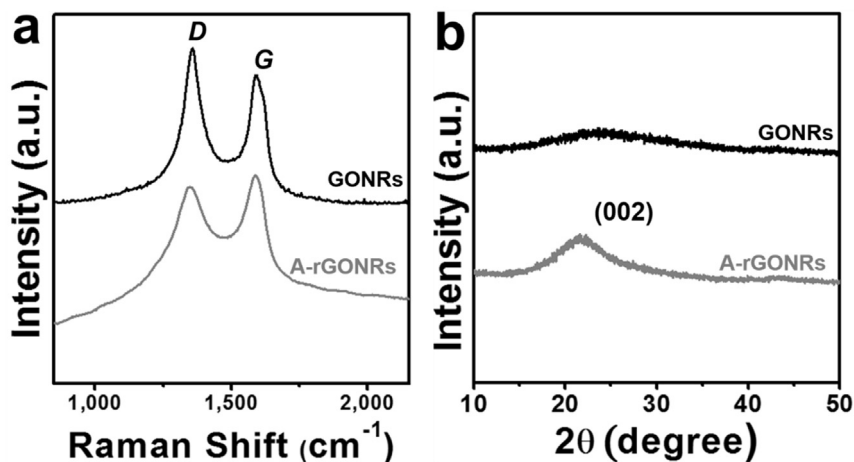
Fig. 2. (a) Raman spectra and (b) XRD patterns of GONRs and A–rGONRs.

stored in a convection oven at 30 °C. The nanocomposite samples were named NC-0.05, -0.1, and -0.3, referring to the A-rGONRs content.

2.4. Characterization

The morphology of the samples was examined using field-emission scanning electron microscopy (FE-SEM, S-4300, Hitachi, Tokyo, Japan) and field-emission transmission electron microscopy

(FE-TEM, JEM2100F, JEOL, Tokyo, Japan). The Raman spectra were recorded using a continuous-wave linearly polarized laser (wavelength: 514.5 nm; 2.41 eV; power: 16 mW). X-ray diffraction (XRD, Rigaku DMAX 2500) was performed using Cu-Kα radiation (wavelength λ = 0.154 nm) with an instrument operated at 40 kV and 100 mA. The laser beam was focused via a 100× objective lens, resulting in a spot diameter of approximately 1 μm. The acquisition time was 10 s and three cycles were required to collect each spectrum. The chemical composition of the samples was examined
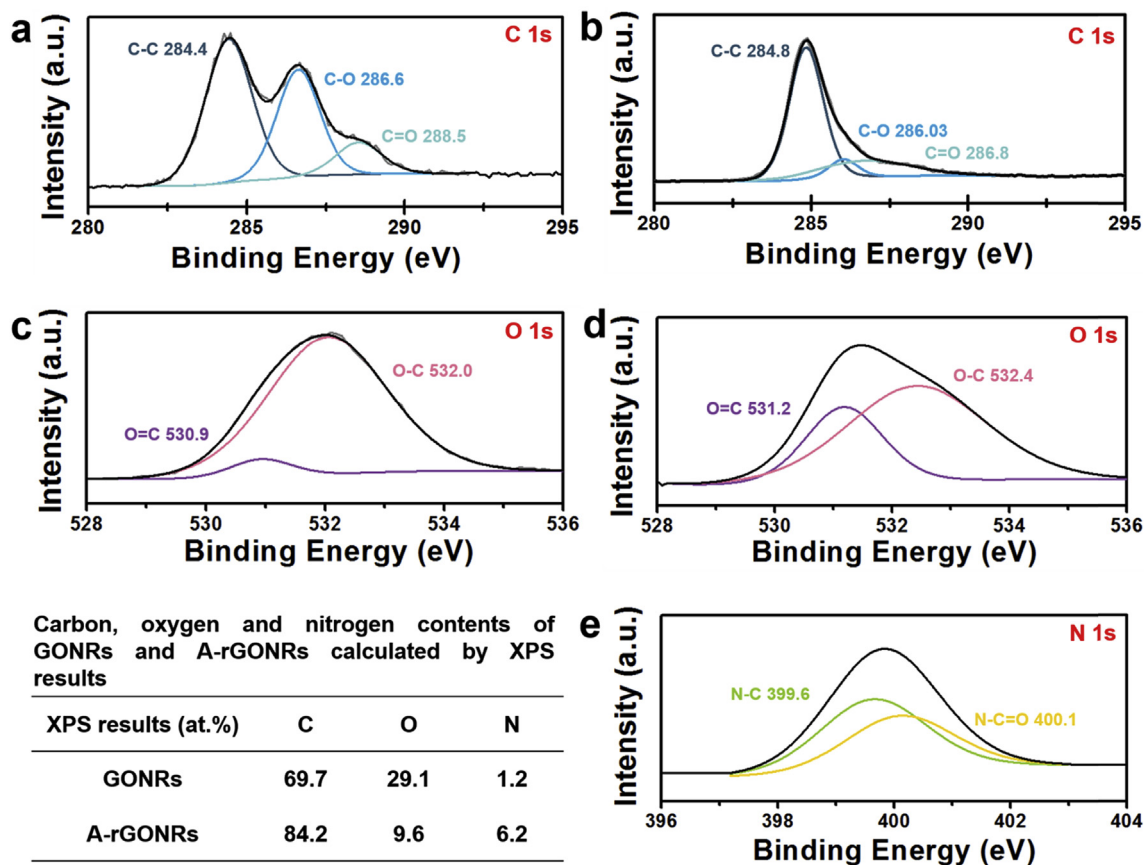

XPS results (at.%)	C	O	N
GONRs	69.7	29.1	1.2
A-rGONRs	84.2	9.6	6.2

Carbon, oxygen and nitrogen contents of GONRs and A-rGONRs calculated by XPS results

Fig. 3. XPS C 1s spectra of (a) GONRs and (b) A-rGONRs; O 1s spectra of (c) GONRs and (d) A-rGONRs; and N 1s spectra of (e) A-rGONRs. (A colour version of this figure can be viewed online.)
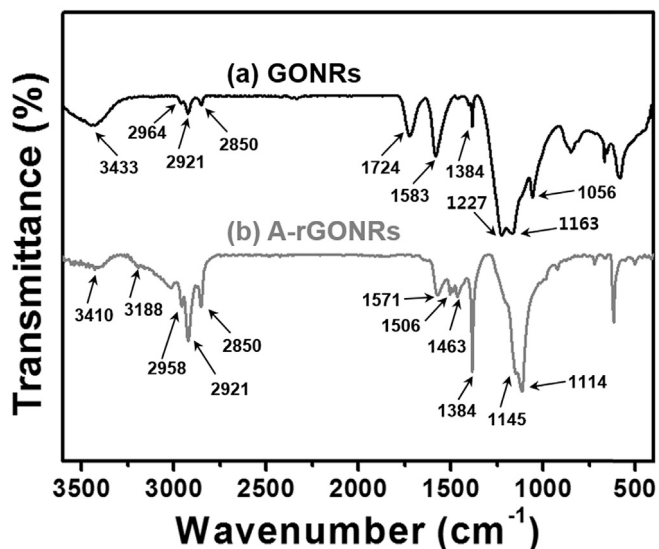
Fig. 4. FT-IR spectra of (a) GONRs and (b) A-rGONRs.

using X-ray photoelectron spectroscopy (XPS, PHI 5700 ESCA, Chanhassen, MN, USA) with monochromatic Al-Kα radiation (hν = 1486.6 eV). The bonding chemistry of GONRs and A-rGONRs was examined via Fourier transform infrared spectroscopy (FT-IR, VERTEX 80v, Bruker Optics, Germany). The thermal degradation behaviors of the nanocomposites were calculated via thermogravimetric analysis (TGA, Q50, TA instruments, UK) at temperatures ranging from 20 to 800 °C at a heating rate of 10 °C min^{-1} under a nitrogen atmosphere. The contact angle data of GONR and A-rGONR films were obtained using automatic contact angle equipment (Phoenix 300, Korea). Differential scanning calorimetry (DSC, Perkin-Elmer 7) was carried out in dry nitrogen gas at a flow rate of 10 mL min^{-1}. The DSC was calibrated using indium as the standard, and the sample weight was 5.0 ± 0.1 mg. The thermal history of the products was removed by scanning them from 30 to 220 °C at a heating rate of 10 °C min^{-1} followed by cooling to 25 °C at a scan rate of 10 °C min^{-1}. The tensile properties were tested using an Instron 4665 ultimate tensile testing machine (UTM) at 20 °C and 30% humidity. The dumb-bell specimens were made in accordance with the ASTM D 638 standard for tensile testing. The cross-head speed was set to 50 mm min^{-1} for both the dumb-bell samples. The mean value of each product was determined as the average value of the five test specimens. The specific dispersion behaviors of A-rGONRs in xylene were characterized via Turbiscan (Formulaction, France) with a wavelength of 880 nm. The electrical conductivity of the samples was tested using an electrical conductivity meter (Loresta GP, Mitsubishi Chemical, Japan).

3. Results and discussion

MWCNTs with high aspect ratios (>100) and high persistence length (l_{sp}, ~520 nm) were used to prepare GONRs via an unzipping process, as shown in Fig. S2 [6,38]. The morphologies of the prepared GONRs are shown in Fig. 1(a–c). The GONRs have a width of approximately 30–50 nm and high aspect ratios (>100). The high-resolution FE-TEM image in Fig. 1(d) shows that the GONRs have an amorphous carbon structure. GONRs were reacted with octylamine in distilled water and a xylene mixture solution at 130 °C using a Dean-Stark trap [See Fig. S1]. In this process, distilled water and xylene were evaporated through a fractionating column and condensed in a reflux condenser. The condensed droplets then passed through a burette filled with xylene, as shown in Fig. S1. The water droplets sank to the bottom of the burette, because of their relatively high density compared to xylene. After several hours, water was fully removed in the round-bottom flask. The reaction progressed via a simple route between octylamine dissolved in xylene and GONRs dispersed in water. The reaction occurred at the interface of the solvents. The epoxide and carboxylic acid groups of GONRs underwent nucleophilic attack by octylamine molecules. As a result, a homogeneous A-rGONR dispersion in xylene was obtained. In addition, the defective carbon structure of GONRs could be restored by the reaction process, because the reaction temperature was high enough to thermally reduce the GONRs. FE-SEM and FE-TEM images of the A-rGONRs show morphologies similar to those of GONRs [Fig. 1(e–g)], indicating that the one-step alkylation/reduction step does not affect their morphologies. The high-resolution FE-TEM image in Fig. 1(h) indicates that A-rGONRs have amorphous carbon structures. However, A-rGONRs have a more ordered hexagonal carbon structure than GONRs, which is confirmed from the higher magnification images in Figs. S3–S6 and the selected area diffraction patterns in Fig. S7. Further, the specific carbon structure of the samples was determined from Raman spectra and XRD patterns. The Raman spectra of the GONRs and A-rGONRs clearly show the main D and G bands. The D band represents the intrinsic phonon mode with A$_{1g}$ symmetry of the infinite aromatic ring that is activated by the structural disorder, and the G band reflects the hexagonal structure related to the E$_{2g}$ vibration mode of the sp^2-hybridized C atoms. The I_G/I_D intensity ratios of GONRs and A-rGONRs are 0.82 and 1.10, respectively [Fig. 2(a)], indicating that A-rGONRs have an ordered hexagonal carbon structure.

The XRD pattern of the GONRs shows no distinct peak, indicating poor development of the graphitic structure [Fig. 2(b)]. In contrast, the XRD pattern of A-rGONRs exhibits a broad graphite (002) peak at 22.3°, indicating that the A-rGONRs have nanometer-scale graphitic layers [Fig. 2(b)]. The restoration of the aromatic hexagonal carbon structure is further investigated by obtaining the electrical conductivities of the A-rGONR and GONR films. The A-rGONR films showed an electrical conductivity of 2.4×10^{-1} S cm^{-1}, which is four orders of magnitude higher than that of GONR-based films (5.5×10^{-5} S cm^{-1}), supporting the results obtained from the Raman spectra and XRD patterns.

Changes in the chemical structure following the chemical reaction were investigated using XPS and IR spectroscopy, as shown
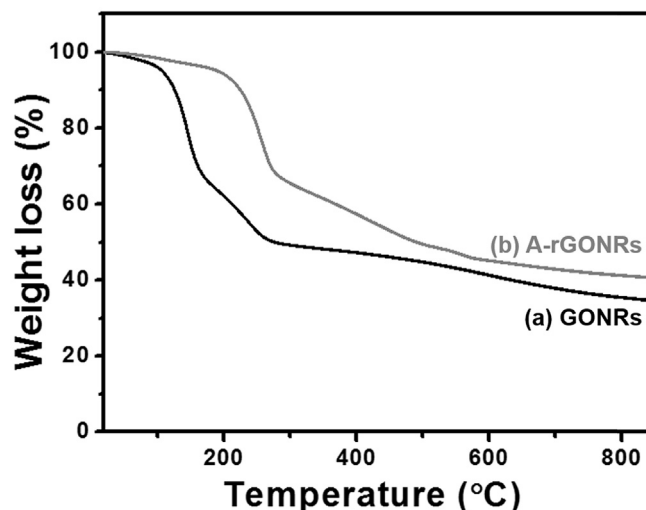

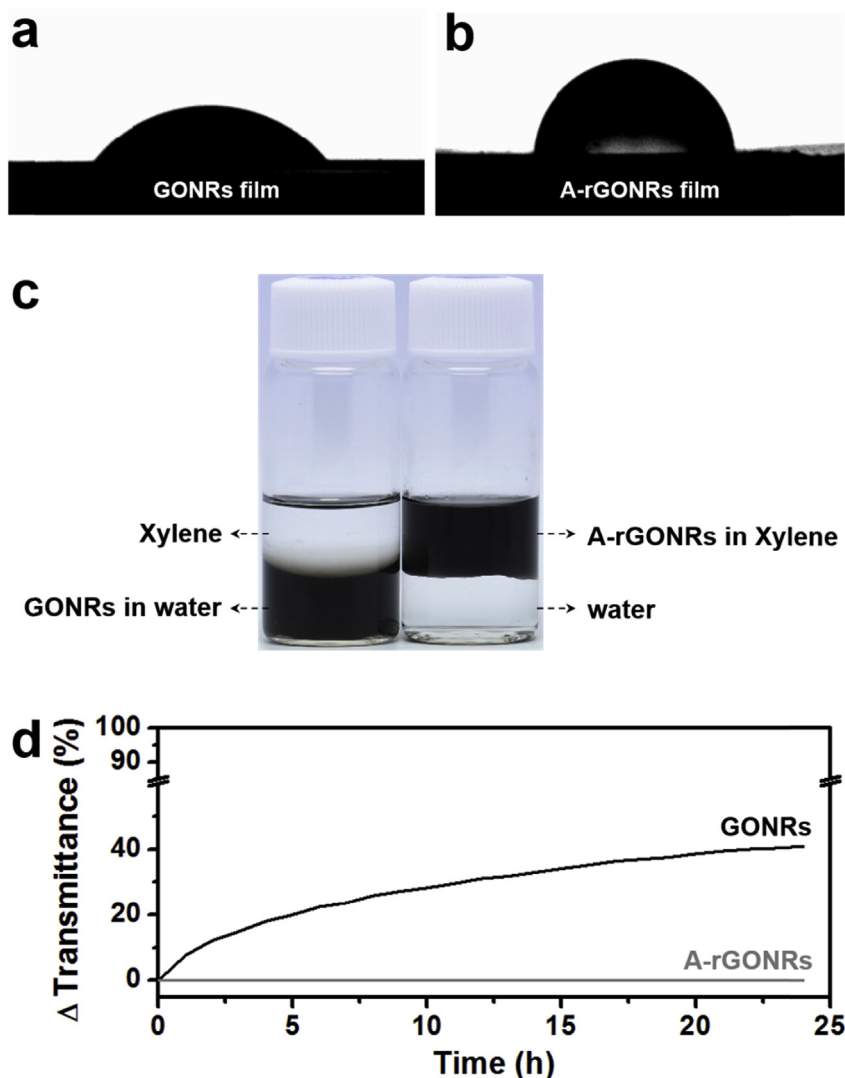**Fig. 5.** TGA curves of (a) GONRs and (b) A-rGONRs.

Fig. 6. Contact angle data of water on (a) GONRs and (b) A-rGONR film. (c) Photographs of dispersion behaviors of GONRs and A-rGONRs in a xylene and water mixture solution. (d) Time vs. transmittance variation plot of GONRs and A-rGONRs dispersions in xylene obtained from Turbiscan®. (A colour version of this figure can be viewed online.)

in Figs. 3 and 4, respectively. Several distinct peaks were observed in the XPS C 1s spectrum of GONRs, such as the main C—C bonding centered at 284.4, C—O bonding centered at 286.6 eV, and C=O bonding centered at 288.5, as shown in Fig. 3(a). Although these three peaks were also found in the XPS C 1s spectrum of A-rGONRs, the intensities of the C—O bonding and C=O bonding were considerably decreased, as shown in Fig. 3(b). This tendency was also observed in the XPS O 1s spectra of GONRs and A-rGONRs. Two peaks, the C=O bonding and C—O bonding centered at 530.9 eV and 532.0 eV, were confirmed in the XPS O 1s spectrum of the GONRs shown in Fig. 3(c). Two similar peaks were observed in the XPS O 1s spectrum of A-rGONRs shown in Fig. 3(d); however, the relative intensity ratio of the C—O to C=O bonding was dramatically decreased in the XPS O 1s spectrum of the A-rGONRs. This data confirms the reduction of GONRs during the chemical reaction process. C—O bonding in particular was dramatically reduced in the reaction process. As mentioned above, octylamine reacted with epoxide groups on GONRs via nucleophilic attack on the amine. This reaction induced a nucleophilic addition of alkyl groups to the surface of the GONRs and simultaneously removed oxygen groups there. Also, the high reaction temperature (130 °C) induced the reduction of GONRs. The oxygen content, calculated from the XPS

results, decreased significantly from 29.1 at.% (GONRs) to 9.6 at.% (A-rGONRs) [Fig. 3]. Nitrogen atoms of ~5.0 at.% were introduced on the A-rGONRs. These have two different chemical bonding structures, C—N bonding centered at 399.6 eV and N—C=O bonding centered at 400.1 eV [Fig. 3(e)]. The increased number of nitrogen atoms introduced on the surface of the GONRs can be considered as direct evidence for the alkylation of octylamine on the GONRs.

The IR spectra of the GONRs and A-rGONRs support the XPS results [Fig. 4]. The presence of hydroxyl, carboxyl, epoxide, and ether groups was observed at 3433, 1724, 1227, and 1163 cm^{-1} respectively, in the IR spectrum of GONRs. In contrast, the intensity of the hydroxyl groups decreased and carboxyl groups were not found in the IR spectrum of the A-rGONRs. Peak intensities relating to C—H bonding such as 2964, 2921, 2850, and 1384 cm^{-1} increased. The specific peak assignments are shown in Table S1.

The composition of the alkyl chains introduced onto the A-rGONRs was estimated using the TGA curve shown in Fig. 5. For GONRs, the first prominent weight loss of ~28% occurred between 100 and 170 °C, which was due to the decomposition of oxygen-containing functional groups. The second significant weight loss of ~18% in the temperature range 170–270 °C is believed to be caused by pyrolysis of defective carbon structures. In contrast, the
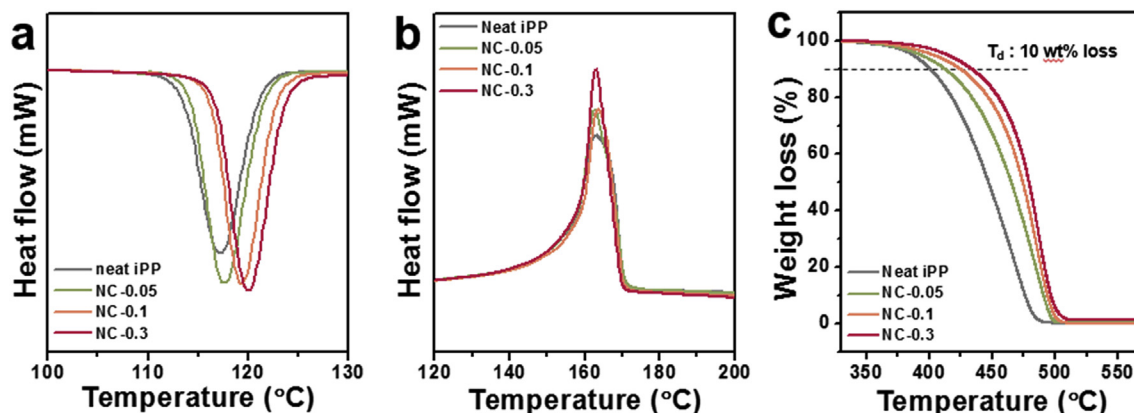
Fig. 7. DSC data of neat iPP, NC-0.05, -0.1, and -0.3 for (a) T_c and (b) T_m. (c) TGA curves of neat iPP, NC-0.05, -0.1, and -0.3. (A colour version of this figure can be viewed online.)

Table 1
Thermal properties of neat iPP, NC-0.05, -0.1, and -0.3 characterized via DSC and TGA.

Sample	T_c (°C)	T_m (°C)	T_d (°C)
Neat iPP	117.2	163.1	401.4
NC-0.05	117.6	162.7	411.9
NC-0.1	119.4	163.6	424.0
NC-0.3	120.1	162.9	432.4

curve of the A-rGONRs show a prominent weight loss of ~25% in the temperature range of 210–290 °C, which could be caused by thermal degradation of the alkyl groups introduced during the re-action. Subsequent weight loss arising from the pyrolysis of carbon structures progressed in the broad temperature range of 290–600 °C. These results show that oxygen-containing functional groups on A-rGONRs are already removed during the reaction process, and A-rGONRs are more thermally stable than GONRs.

The hydrophobicity of GONRs and A-rGONRs was confirmed by examining the contact angle of a water droplet on A-rGONR-based films [Fig. 6(a) and (b)]. The contact angle between the A-rGONR-based film and the water droplet was 88.4°, which is larger than that between the GONRs and the water droplet (58.2°). The surface energy was calculated from the contact angle values of GONRs (52.4 mJ m^{-2}) and A-rGONRs (23.8 mJ m^{-2}). The surface energy of the A-rGONRs is close to that of xylene (28.90 mJ m^{-2} at 20 °C), which means that A-rGONRs can be readily dispersed in xylene. A dispersion stability test between A-rGONRs and GONRs [Fig. 6(c)]

was carried out, and a stable colloidal suspension of A-rGONRs was achieved in xylene even after 24 h [Fig. 6(d)]. These results indicate that the octylamine alkyl groups effectively improve the miscibility between A-rGONRs and xylene, which is a good solvent for iPP. It is therefore expected that A-rGONRs will be compatible with the iPP matrix.

The thermal properties of neat iPP, NC-0.05, -0.1, and -0.3 were investigated using DSC tests (Fig. 7 and Table 1). Fig. 7(a) shows the DSC cooling curves, which provided the crystallization temperature (T_c) relative to the content of A-rGONRs in the iPP matrix. The crystallization onset temperature gradually increased with the loading content of A-rGONRs. Alkyl groups on the A-rGONRs can improve the interaction with iPP chains, hence the function of A-rGONRs as nucleating agents can be demonstrated. The T_c of the nanocomposites increased to ~2.9 °C in NC-0.3. In contrast, the melting temperature of the nanocomposites was similar [Fig. 7(b)], indicating that the A-rGONRs do not affect the thermal transition of the crystal structure of iPP. The T_d of the nanocomposites gradually increased with the A-rGONRs content. The addition of just 0.3 wt% of A-rGONRs, increased the T_d by ~31 °C from 401 to 432 °C, compared to the T_d of neat iPP. These results are superior to those of iPP nanocomposites based on alkylated graphene oxide, which showed an increase of ~16 °C at the same loading content (0.3 wt%) [31]. Also, compared with the T_d (~424 °C) of rGONR-based iPP nanocomposites, A-rGONRs showed improved reinforcing effects [Fig. S8 and Table S2]. The significant enhancement in thermal properties could be a result of the efficient thermal dissipation and free-radical scavenging effects of A-rGONRs in the nanocomposites.
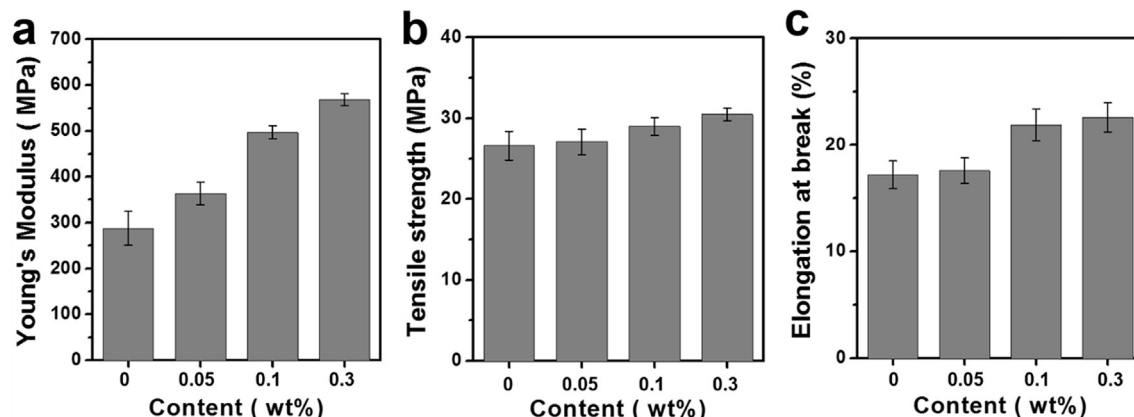

Fig. 8. Mechanical properties including (a) Young's modulus, (b) tensile strength, and (c) elongation at the break of neat iPP, NC-0.05, -0.1, and -0.3.

Table 2
Mechanical properties of neat iPP, NC-0.05, -0.1, and -0.3 characterized via UTM.

Sample	Young's modulus (MPa)	Tensile strength (MPa)	Elongation at break (%)
Neat iPP	287.4 ± 36.9	26.6 ± 1.8	17.2 ± 1.3
NC-0.05	363.2 ± 25.0	27.1 ± 1.6	17.6 ± 1.2
NC-0.1	497.0 ± 14.2	29.0 ± 1.1	21.9 ± 1.5
NC-0.3	569.0 ± 13.1	30.5 ± 0.8	22.6 ± 1.4

Also, the high aspect ratio and one-dimensional morphologies of A-rGONRs could lead to a percolation threshold with low loading content, indicating that the reinforcing effects were achieved efficiently via the use of A-rGONRs.

The mechanical properties of the nanocomposites were investigated via UTM tests [Fig. 8]. The Young's modulus of the nanocomposites (287.4 ± 36.9 MPa) increased significantly with the addition of A-rGONRs over that of neat iPP. NC-0.05, NC-0.1 and NC-0.3 showed Young's modulus values of 363.2 ± 25.0, 497.0 ± 14.2, and 569.0 ± 13.1 MPa, respectively. The increasing ratios correspond to 26.4, 72.9, and 98.0% for NC-0.05, NC-0.1, and NC-0.3, respectively. The tensile strength of the nanocomposites increased from 26.6 ± 1.8 MPa of neat iPP to 30.5 ± 0.8 MPa of NC-0.3, which corresponds to an increase of ~15%. One interesting observation, when the A-rGONRs were introduced to the nanocomposites, was the increased elongation at the break. With the

addition of A-rGONRs, elongation values increased by ~22.6%. The increases in both strength and elongation indicate enhanced toughness, of which the neat iPP, NC-0.05, NC-0.1 and NC-0.3 are calculated as 296, 336, 448 and 508 MPa, respectively. More specific information about the mechanical properties of the nanocomposites is given in Table 2. The reinforcing effects of A-rGONRs on mechanical properties are superior to those of rGONRs at the same loading content [Fig. S9 and Table S2]. These improved mechanical properties are attributed to good interfacial adhesion between the neat iPP matrix and the A-rGONRs, which have a higher modulus and strength than that of the iPP matrix. The A-rGONRs have large interfacial areas, high aspect ratios, and numerous alkyl groups, which allows them to strongly interlock with the iPP matrix. The reinforcing effects can be maximized via the homogeneous dispersion of A-rGONRs into the iPP matrix. With the application of a tensile load to the nanocomposites, crack initiation can occur at
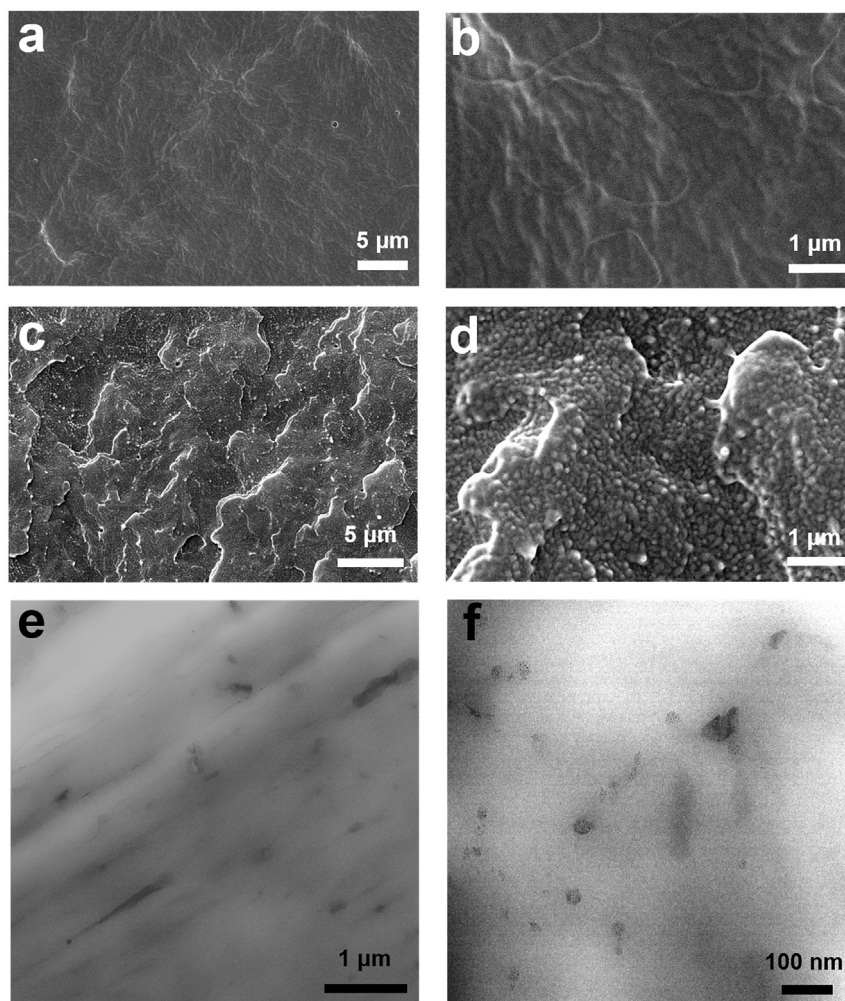

Fig. 9. FE-SEM images for a fractured cross-section of (a), (b) neat iPP and (c), (d) NC-0.1. (e), (f) FE-TEM images with various magnifications prepared by microtoming NC-0.1.

low A-rGONRs density areas; therefore, provided that the A-rGONRs are homogeneously and randomly distributed in the matrix, the load transfer from the matrix to the A-rGONRs is probably more effective. This will result in increased tensile strength and elongation at the break. The dispersibility of A-rGONRs in the iPP matrix was confirmed using FE-SEM, as shown in Fig. 9(a−d). While the fracture surface of the iPP matrix is smooth [Fig. 9(a) and (b)], NC-0.1 has a rough fracture surface [Fig. 9(c) and (d)]. Also, homogeneously dispersed A-rGONRs in the iPP matrix were observed, as shown in Fig. 9(c) and (d). FE-TEM images support homogeneous dispersion in the iPP matrix, in which the presence of individual A-rGONRs is confirmed [Fig. 9(e) and (f)].

4. Conclusion

A-rGONRs were prepared by unzipping MWCNTs with high aspect ratios (>100) and high persistence lengths (l_{sp}, ~520 nm), followed by alkylation and reduction via a simple method using a Dean-Stark trap. A-rGONRs have a width of approximately 30−50 nm, high aspect ratios (>100), and microstructures composed of nanometer-scale graphitic layers. Approximately 25% of alkyl groups were introduced onto the surface of A-rGONRs, leading to hydrophobic properties with a surface energy of 23.8 mJ m^{-2}. A stable colloidal suspension of A-rGONRs was achieved in xylene even after 24 h, because the surface energy is similar to that (28.90 mJ m^{-2} at 20 °C) of xylene, which is a good solvent for iPP. For NC-0.05, -0.1, and -0.3, A-rGONRs were homogeneously dispersed into the iPP matrix and showed significant reinforcing effects on the thermal and mechanical properties of the iPP matrix. When the ~0.3 wt% A-rGONRs were introduced in the iPP host, the T_c and T_d of iPP increased by ~2.9 °C and ~31 °C, respectively. Also, the Young's modulus, tensile strength, elongation, and toughness of the iPP matrix increased by approximately 98.0, 15, 22.6, and 43.5%, respectively, by adding ~0.3 wt% A-rGONRs.

Acknowledgments

Appendix A. Supplementary data

Supplementary data related to this article can be found at http://dx.doi.org/10.1016/j.carbon.2016.07.020.

References

[1] D. Li, M.B. Müeller, S. Gilje, R.B. Kaner, G.G. Wallace, Processable aqueous dispersions of graphene nanosheets, Nat. Nanotechnol. 3 (2) (2008) 101−105.

[2] C. Lee, X. Wei, J.W. Kysar, J. Hone, Measurement of the elastic properties and intrinsic strength of monolayer graphene, Science 321 (5887) (2008) 385−388.

[3] M.F. Yu, O. Lourie, M.J. Dyer, K. Moloni, T.F. Killy, R.S. Ruoff, Strength and breaking mechanism of multiwalled carbon nanotubes under tensile load, Science 287 (5453) (2000) 637−640.

[4] A.A. Balandin, S. Ghosh, W. Bao, I. Calizo, D. Teweldebrhan, F. Miao, et al., Superior thermal conductivity of single-layer graphene, Nano Lett. 8 (3) (2008) 902−907.

[5] M. Martin-Gallego, R. Verdejo, M. Khayet, J.M.O. de Zarate, M. Essalhi, M.A. Lopez-Manchado, Thermal conductivity of carbon nanotubes and graphene in epoxy nanofluids and nanocomposites, Nanoscale Res. Lett. 6 (1) (2011) 1−7.

[6] Y.S. Yun, G. Yoon, K. Kang, H.-J. Jin, High-performance supercapacitors based on defect-engineered carbon nanotubes, Carbon 80 (2014) 246−254.

[7] B. Safadi, R. Andrews, E.A. Grulke, Multiwalled carbon nanotube polymer composites: synthesis and characterization of thin films, J. Appl. Polym. Sci. 84 (14) (2002) 2660−2669.

[8] M. Cadek, J.N. Coleman, V. Barron, K. Hedicke, W.J. Blau, Morphological and mechanical properties of carbon-nanotube-reinforced semicrystalline and amorphous polymer composites, Appl. Phys. Lett. 81 (27) (2002) 5123−5125.

[9] C. Velasco-Santos, A.L. Martínez-Hernández, F.T. Fisher, R. Ruoff, V.M. Castano, Improvement of thermal and mechanical properties of carbon nanotube composites through chemical functionalization, Chem. Mat. 15 (23) (2003) 4470−4475.

[10] M.S.P. Shaffer, A.H. Windle, Fabrication and characterization of carbon nanotube/poly (vinyl alcohol) composites, Adv. Mater 11 (11) (1999) 937−941.

[11] J.N. Coleman, M. Cadek, R. Blake, V. Nicolosi, K.P. Ryan, C. Belton, et al., High-performance nanotube-reinforced plastics: understanding the mechanism of strength increase, Adv. Funct. Mater 14 (8) (2003) 791−798.

[12] S. Stankovich, D.A. Dikin, G.H.B. Dommett, K.M. Kohlhaas, E.J. Zimney, E.A. Stach, et al., Graphene-based composite materials, Nature 442 (7100) (2006) 282−286.

[13] J. Liang, Y. Huang, L. Zhang, Y. Wang, Y. Ma, T. Guo, et al., Molecular-level dispersion of graphene into poly (vinyl alcohol) and effective reinforcement of their nanocomposites, Adv. Funct. Mater 19 (14) (2009) 2297−2302.

[14] Y. Xu, W. Hong, H. Bai, C. Li, G. Shi, Strong and ductile poly (vinyl alcohol)/graphene oxide composite films with a layered structure, Carbon 47 (15) (2009) 3538−3543.

[15] M.A. Rafiee, J. Rafiee, Z. Wang, H. Song, Z.-Z. Yu, N. Koratkar, Enhanced mechanical properties of nanocomposites at low graphene content, ACS Nano 3 (12) (2009) 3884−3890.

[16] Y.S. Yun, V.-D. Le, H. Kim, S.-J. Chang, S.J. Baek, S. Park, et al., Effects of sulfur doping on graphene-based nanosheets for use as anode materials in lithium-ion batteries, J. Power Sources 262 (2014) 79−85.

[17] M.-C. Hsiao, S.-H. Liao, Y.-F. Lin, C.-A. Wang, N.-W. Pu, H.-M. Tsai, et al., Preparation and characterization of polypropylene-graft-thermally reduced graphite oxide with an improved compatibility with polypropylene-based nanocomposite, Nanoscale 3 (4) (2011) 1516−1522.

[18] Q. Su, S. Pang, V. Alijani, C. Li, X. Feng, K. Müllen, Composites of graphene with large aromatic molecules, Adv. Mater 21 (31) (2009) 3191−3195.

[19] E.-Y. Choi, T.H. Han, J. Hong, J.E. Kim, S.H. Lee, H.W. Kim, et al., Noncovalent functionalization of graphene with end-functional polymers, J. Mater. Chem. 20 (10) (2010) 1907−1912.

[20] Q. Yang, X. Pan, F. Huang, K. Li, Fabrication of high-concentration and stable aqueous suspensions of graphene nanosheets by noncovalent functionalization with lignin and cellulose derivatives, J. Phys. Chem. C 114 (9) (2010) 3811−3816.

[21] H.K.F. Cheng, N.G. Sahoo, Y.P. Tan, Y. Pan, H. Bao, L. Li, et al., Poly (vinyl alcohol) nanocomposites filled with poly (vinyl alcohol)-grafted graphene oxide, ACS Appl. Mater. Interfaces 4 (5) (2012) 2387−2394.

[22] H.J. Salavagione, M.A. Gomez, G. Martínez, Polymeric modification of graphene through esterification of graphite oxide and poly (vinyl alcohol), Macromolecules 42 (17) (2009) 6331−6334.

[23] O.C. Compton, D.A. Dikin, K.W. Putz, L.C. Brinson, S.T. Nguyen, Electrically conductive "alkylated" graphene paper via chemical reduction of amine-functionalized graphene oxide paper, Adv. Mater 22 (8) (2010) 892−896.

[24] S. Stankovich, R.D. Piner, S.T. Nguyen, R.S. Ruoff, Synthesis and exfoliation of isocyanate-treated graphene oxide nanoplatelets, Carbon 44 (15) (2006) 3342−3347.

[25] S. Stankovich, D.A. Dikin, R.D. Piner, K.A. Kohlhaas, A. Kleinhammes, Y. Jia, et al., Synthesis of graphene-based nanosheets via chemical reduction of exfoliated graphite oxide, Carbon 45 (7) (2007) 1558−1565.

[26] T. Ramanathan, A.A. Abdala, S. Stankovich, D.A. Dikin, M. Herrera-Alonso, R.D. Piner, et al., Functionalized graphene sheets for polymer nanocomposites, Nat. Nanotechnol. 3 (6) (2008) 327−331.

[27] T.H. Vo, M. Shekhirev, D.A. Kunkel, M.D. Morton, E. Berglund, L. Kong, et al., Large-scale solution synthesis of narrow graphene nanoribbons, Nat. Commun. 5 (2014) 3189.

[28] D.V. Kosynkin, A.L. Higginbotham, A. Sinitskii, J.R. Lomeda, A. Dimiev, B. Katherine Price, et al., Longitudinal unzipping of carbon nanotubes to form graphene nanoribbons, Nature 458 (7240) (2009) 872−876.

[29] A. Bianco, H.-M. Cheng, T. Enoki, Y. Gogotsi, H. Hurt, N. Koratkar, et al., All in the graphene family—a recommended nomenclature for two-dimensional carbon materials, Carbon 65 (2013) 1−6.

[30] M.A. Rafiee, W. Lu, A.V. Thomas, A. Zandiatashbar, J. Rafiee, J.M. Tour, et al., Graphene nanoribbon composites, ACS Nano 4 (12) (2010) 7415−7420.

[31] Y.S. Yun, Y.H. Bae, D.H. Kim, J.Y. Lee, I.-J. Chin, H.-J. Jin, Reinforcing effects of adding alkylated graphene oxide to polypropylene, Carbon 49 (11) (2011) 3553−3559.

[32] H. Kim, A.A. Abdala, C.W. Macosko, Graphene/polymer nanocomposites, Macromolecules 43 (16) (2010) 6515−6530.

[33] B. Philip, J. Xie, J.K. Abraham, V.K. Varadan, A new synthetic route to enhance polyaniline assembly on carbon nanotubes in tubular composites, Smart Mater. Struct. 13 (6) (2004) N105−N108.

[34] A. Dimiev, D. Zakhidov, B. Genorio, K. Oladimeji, B. Crowgey, L. Kempel, et al., Permittivity of dielectric composite materials comprising graphene nanoribbons. The effect of nanostructure, ACS Appl. Mater. Interfaces 5 (15) (2013)

7567–7573.

[35] C. Xiang, P.J. Cox, A. Kukovecz, B. Genorio, D.P. Hashim, Z. Yan, et al., Functionalized low defect graphene nanoribbons and polyurethane composite film for improved gas barrier and mechanical performances, ACS Nano 7 (11) (2013) 10380–10386.

[36] R. Nadiv, M. Shtein, M. Buzaglo, S. Peretz-Damari, A. Kovalchuk, T. Wang, et al., Graphene nanoribbon–Polymer composites: The critical role of edge

functionalization, Carbon 99 (2016) 444–450.

[37] M.Y. Song, Y.S. Yun, N.R. Kim, H.-J. Jin, Dispersion stability of chemically reduced graphene oxide nanoribbons in organic solvents, RSC Adv. 6 (23) (2016) 19389–19393.

[38] H.S. Lee, C.H. Yun, H.M. Kim, C.J. Lee, Persistence length of multiwalled carbon nanotubes with static bending, J. Phys. Chem. C 111 (51) (2007) 18882–18887.